Ferroelectric tuning of the valley polarized metal-semiconductor transition in $Mn_2P_2S_3Se_3/Sc_2CO_2$ van der Waals heterostructures and application to nonlinear Hall effect devices

Hanbo Sun,[1,‡] Yewei Ren,[1,‡] Chao Wu,[1] Pengqiang Dong,[1] Weixi Zhang,[2,†] Yin-Zhong Wu,[3] and Ping Li[1,4,5,*]

[1] *State Key Laboratory for Mechanical Behavior of Materials, School of Materials Science and Engineering, Xi'an Jiaotong University, Xi'an, Shaanxi 710049, People's Republic of China*

[2] *Department of Physics and Electronic Engineering, Tongren University, Tongren 554300, People's Republic of China*

[3] *School of Physical Science and Technology, Suzhou University of Science and Technology, Suzhou 215009, People's Republic of China*

[4] *State Key Laboratory for Surface Physics and Department of Physics, Fudan University, Shanghai 200433, People's Republic of China*

[5] *State Key Laboratory of Silicon and Advanced Semiconductor Materials, Zhejiang University, Hangzhou 310027, People's Republic of China*

(Received 6 September 2024; revised 12 January 2025; accepted 7 March 2025; published 14 March 2025)

To promote the development of the next generation of nanospintronic devices, it is of great significance to tune the valley degree of freedom in two-dimensional (2D) materials. Here, we propose a mechanism for manipulating the valley and nonlinear Hall effect using a 2D ferroelectric substrate. Monolayer $Mn_2P_2S_3Se_3$ is a robust antiferromagnetic, valley polarized semiconductor. Importantly, the valley polarized metal-semiconductor phase transition of $Mn_2P_2S_3Se_3$ can be effectively tuned by switching the ferroelectric polarization of Sc_2CO_2. We reveal the microscopic mechanism of the phase transition, which originates from charge transfer and band alignment. Additionally, we find that the reversed polarization direction of Sc_2CO_2 can flexibly manipulate the Berry curvature dipole. Based on this discovery, we present the detection of the valley polarized metal-semiconductor transition using nonlinear Hall effect devices. These findings not only offer a scheme to tune the valley degree of freedom but also provide a promising platform for designing nonlinear Hall effect devices.

DOI: 10.1103/PhysRevApplied.23.034032

I. INTRODUCTION

Limited by the storage wall problem and the von Neumann bottleneck, traditional silicon-based memory cannot meet the demands of massive data processing and storage [1,2]. Therefore, revolutionary ultrafast, nonvolatile memory technologies with low power consumption and ultrahigh capacity, based on alternative mechanisms, structures, and materials, are highly sought after [3–6]. Among the potential candidates, the rapid development of two-dimensional (2D) materials and their heterojunctions provides promising opportunities due to their ideal atomic-level flatness without dangling bonds, unique electronic properties, and high adjustability [7–10].

Recently, the concept of ferrovalley materials with spontaneous valley polarization was proposed by Tong *et al.* [11]. Ferrovalley materials combine the valley degree of freedom with ferroic order [12–16]. Consequently, they have not only valley-degree-of-freedom features but also magnetic or ferroelectric characteristics. They have potential applications in information storage, processing, and transmission based on the coding and probing of the valley (spin) degree of freedom; they can be used to construct valley (spin) valves, valley (spin) filters, and valleytronic (spintronic) devices [17–20]. A large number of ferrovalley materials have been reported, including FeX_2 (X = Cl, Br) [21,22], Cr_2Se_3 [23], XY (X = K, Rb, Cs; Y = N, P, As, Sb, Bi) [24], YI_2 [25], $VSiXN_4$ (X = C, Si, Ge, Sn, Pb) [26], and Fe_2CF_2 [27]. While it is predicted that a large number of ferrovalley materials exist, achieving nonvolatile valley control is key to realizing valleytronic devices.

Moreover, the nonlinear Hall effect (NHE) has been recently discovered [28,29]. Unlike the linear anomalous Hall effect, where the transverse Hall currents are linearly proportional to the longitudinal driving electric field and

*Contact author: pli@xjtu.edu.cn
†Contact author: zhangwwxx@sina.com
‡These authors contributed equally to this work.

only present in magnetic systems, the transverse Hall voltage of the NHE is quadratic with the driving current, requiring the breaking of spatial inversion (P) symmetry [30–34]. If the system further breaks the time-reversal symmetry (T), how does the NHE change? More importantly, can a 2D ferroelectric substrate effectively tune the nonlinear Hall conductance?

In this work, we propose that the valley polarization and nonlinear Hall conductance of Janus $Mn_2P_2S_3Se_3$ can be tuned using a 2D ferroelectric substrate, Sc_2CO_2. Based on density functional theory (DFT), we comprehensively investigate the magnetic ground state, electronic properties, valleytronic properties, and Berry curvature dipole (BCD) for the $Mn_2P_2S_3Se_3/Sc_2CO_2$ van der Waals (vdW) heterostructure. We find that the valley polarized metal-semiconductor transition of $Mn_2P_2S_3Se_3$ can be effectively achieved by altering the ferroelectric polarization of Sc_2CO_2. Furthermore, switching the of electric polarization can induce the large BCDs. Our findings provide valuable guidance for the future development of valleytronic nanoswitches and NHE devices.

II. COMPUTATIONAL METHODS

All calculations are implemented based on the framework of DFT using the Vienna Ab initio Simulation Package (VASP) [35,36]. The generalized gradient approximation (GGA) with the Perdew-Burke-Ernzerhof functional is used to describe the exchange-correlation energy [37]. The plane-wave basis with a kinetic energy cutoff of 500 eV is employed. A vacuum of 25 Å is set along the c axis to avoid interaction between the sheet and its periodic images. The convergence criteria for the total energy and the force are set to 10^{-6} eV and -0.01 eV/Å, respectively. The zero-damping DFT-D3 method of Grimme *et al.* is considered for the vdW correction in the $Mn_2P_2S_3Se_3/Sc_2CO_2$ heterostructure [38]. To describe strongly correlated $3d$ electrons of Mn, the GGA + U method is applied with the effective U value ($U_{\text{eff}} = U - J$) of 4 eV. To study the dynamical stability, the phonon spectra are calculated using the PHONOPY code using a $4 \times 4 \times 1$ supercell [39]. The maximally localized Wannier functions are used to construct an effective tight-binding Hamiltonian to investigate the Berry curvature and BCD using the WANNIER90 code [40,41]. In the BCD calculations, a k-point mesh grid of $1000 \times 1000 \times 1$ is used to ensure convergence of the results.

III. RESULTS AND DISCUSSION

A. Material model of $Mn_2P_2S_3Se_3/Sc_2CO_2$ van der Waals heterostructures

Before building the atomic models of the $Mn_2P_2S_3Se_3/Sc_2CO_2$ vdW multiferroic heterostructures, we first investigate the crystal structures of monolayer $Mn_2P_2S_3Se_3$ and Sc_2CO_2, as shown in Figs. 1(a), 1(b), 1(d), and 1(e). The monolayer Janus $Mn_2P_2S_3Se_3$ has a hexagonal lattice with the point group C_{3v}, which naturally breaks the P symmetry [42]. Moreover, the asymmetric displacement of the C sublayer relative to the Sc sublayer also results in the breaking of P symmetry for monolayer Sc_2CO_2, inducing out-of-plane ferroelectric polarization [43]. After structural relaxation, the in-plane lattice constants of monolayer $Mn_2P_2S_3Se_3$ and Sc_2CO_2 are 6.25 and 3.42 Å, respectively.

Moreover, we also study the properties of monolayer $Mn_2P_2S_3Se_3$. First, we evaluate its dynamic stability using the phonon-dispersion spectrum. As shown in Fig. 1(c), the absence of imaginary modes along the high-symmetry lines confirms the dynamic stability of monolayer $Mn_2P_2S_3Se_3$. Then, to determine that the Coulomb repulsion U does not effect on the magnetic ground state, we calculate the ferromagnetic (FM) and antiferromagnetic (AFM) states between 1 eV and 5 eV. As listed in Table SI in the Supplemental Material, the total energy of the AFM state is always lower than that of the FM

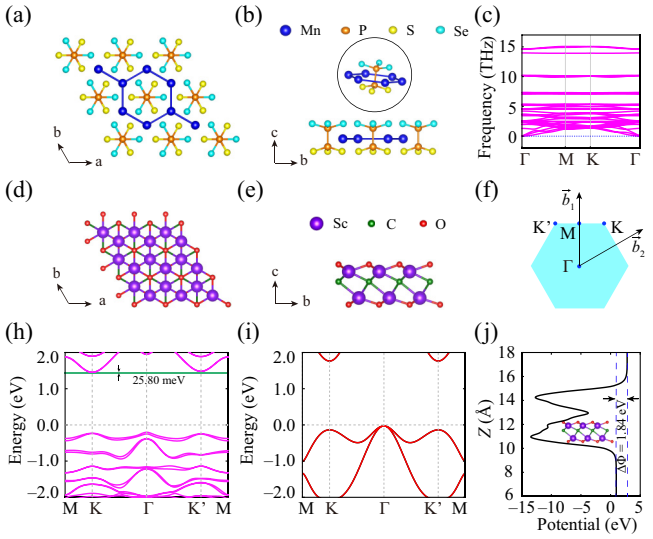

FIG. 1. (a),(b) Top and side views of the crystal structure of monolayer $Mn_2P_2S_3Se_3$, respectively. The dark blue, orange, yellow, and light blue balls represent Mn, P, S, and Se, respectively. (c) Calculated phonon dispersion curves of monolayer $Mn_2P_2S_3Se_3$ along the high-symmetry lines. (d),(e) Top and side views of the crystal structure for monolayer Sc_2CO_2, respectively. The purple, green, and red balls represent Sc, C, and O, respectively. (f) Brillouin zone (BZ) of the honeycomb lattice with the reciprocal lattice vectors $\vec{b}_1$ and $\vec{b}_2$. Here, Γ, K, K′, and M are high-symmetry points in the BZ. (h) Band structure of monolayer $Mn_2P_2S_3Se_3$ considering SOC. The conduction-band valley splitting is indicated by the green shading. (i) Band structure of monolayer Sc_2CO_2 without considering SOC. (j) Plane-averaged electrostatic potential of monolayer Sc_2CO_2, in which $\Delta\Phi$ represents the potential difference.

state [44]. This indicates that the AFM state is robust. The magnetic anisotropy energy (MAE) forms the basis for investigating the properties of magnetic materials. The MAE is defined as the total energy difference between the magnetic moment along the in-plane (E_{100}) and out-of-plane (E_{001}) directions. As listed in Table SI in the Supplemental Material, the Hubbard U has little effect on the MAE [44]. Both are negative, meaning that the direction of easy magnetization is in plane. With such a small MAE, it can be easily tuned out of plane by a small external magnetic field [12]. In previous reports, the Coulomb repulsion U is often taken to be 4 eV for the Mn atom [45,46]. Hence, we choose $U_{\text{eff}} = 4$ eV to investigate all the properties that follow.

For the electronic properties, Fig. S1 [44] in the Supplemental Material and Fig. 1(i) present the band structures of monolayer $Mn_2P_2S_3Se_3$ and Sc_2CO_2 without considering spin-orbit coupling (SOC), respectively. Monolayer $Mn_2P_2S_3Se_3$ appears to be a direct-band-gap semiconductor with a band gap of 1.71 eV located at the K/K′ point. Specifically, spin-up and spin-down channels are degenerate due to the AFM ground state. When SOC is included, as shown in Fig. 1(h), the degeneracy between K and K′ valleys disappears. Simultaneously, the conduction band minimum (CBM) induces a valley splitting of 25.80 meV. Monolayer Sc_2CO_2 is an insulator with an indirect band gap of 1.79 eV. In addition, the out-of-plane polarization of Sc_2CO_2 introduces an electrostatic potential difference of 1.84 eV between the two surfaces of Sc_2CO_2, as shown in Fig. 1(j).

Note that the lattice mismatch is 5.6% for the 1×1 $Mn_2P_2S_3Se_3$ matching to the $\sqrt{3} \times \sqrt{3}$ Sc_2CO_2. Considering that the lattice mismatch rate is large, we optimized the lattice constant of the heterostructure to 5.98 Å. We considered six typical alignments, i.e., the bottom-layer S/Se atom of $Mn_2P_2S_3Se_3$ being in the top and hollow positions of the Sc_2CO_2 honeycomb lattice, respectively. As shown in Fig. 2 and Fig. S2 [44] in the Supplemental Material, we named these the top-O, top-Sc, and hollow configurations. After extensive geometry optimizations, we find that the layer spacing is 2.58–3.45 Å, as listed in Table I. This indicates the nature of the vdW interaction between $Mn_2P_2S_3Se_3$ and Sc_2CO_2. Additionally, to evaluate the stability of these configurations, we calculate the binding energy E_b. This is defined as $E_b = E_{\text{total}} - E_{Mn_2P_2S_3Se_3} - E_{Sc_2CO_2})/N_{S/Se}$, where E_{total}, $E_{Mn_2P_2S_3Se_3}$, and $E_{Sc_2CO_2}$ are the total energies of $Mn_2P_2S_3Se_3/Sc_2CO_2$, $Mn_2P_2S_3Se_3$, and Sc_2CO_2, respectively. Additionally, $N_{S/Se}$ is the number of S/Se atoms at the interface, and E_b is between −161.72 and 286.86 meV, meaning that the configurations are stable and likely to be possible to synthesize experimentally. Importantly, whether the S-surface or Se-surface polarization is upward or downward, the most stable is the top-O configuration.

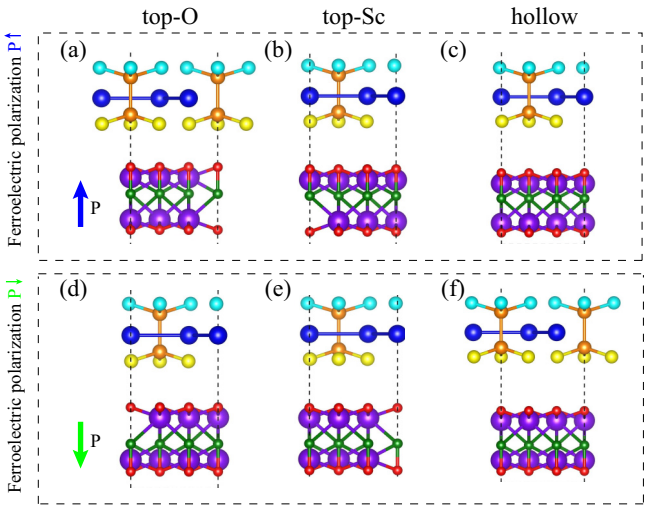

FIG. 2. (a)–(f) Side views of $Mn_2P_2S_3Se_3/Sc_2CO_2$ heterostructures with diverse stacking configurations under different Sc_2CO_2 polarization states. The interface contact is the contact between the S-surface of $Mn_2P_2S_3Se_3$ and Sc_2CO_2. For the (a),(d) top-O, (b),(e) top-Sc, and (c),(f) hollow configurations; (a)–(c) and (d)–(f) show the P↑ and P↓ states, respectively.

B. Ferroelectric tuning of valley polarized metal-semiconductor transition and mechanism

To confirm the magnetic ground state of the $Mn_2P_2S_3Se_3/Sc_2CO_2$ heterostructure, two possible magnetic configurations, the FM and AFM, are considered. The relative energies ($E_{\text{FM}} - E_{\text{AFM}}$) of the FM and AFM phases are listed in Table SII in the Supplemental Material [44]. The energy difference is always positive for all configurations, indicating that the magnetic ground state is the AFM state in the $Mn_2P_2S_3Se_3/Sc_2CO_2$ heterostructure. Furthermore, the MAE of the heterostructure decreases compared to that of the monolayer, as shown in Table SIII in the Supplemental Material [44].

Primarily, we investigate the S-surface. As shown in Fig. S3 in the Supplemental Material, when the SOC is switched off, spin-up and spin-down channels are still degenerate [44]. In the $Mn_2P_2S_3Se_3/Sc_2CO_2$ P↑ case, they exhibit metallic properties, except in the hollow configuration [see Figs. S3(a)–S3(c) in the Supplemental Material] [44]. More interestingly, the greater the binding energy between $Mn_2P_2S_3Se_3$ and Sc_2CO_2, the stronger the metallic properties of the system, as listed in Table I; however, when the ferroelectric polarization of Sc_2CO_2 switches downward, the band gap is opened, and it becomes a semiconductor [see Figs. S3(d)–S3(f) in the Supplemental Material] [44]. When SOC is included, as shown in Figs. 3(a), 3(e), and S4, we find that the CBM of K and K′ points exhibit valley splitting of 35.41–39.10 meV. At this moment, the $Mn_2P_2S_3Se_3/Sc_2CO_2$ P↑ becomes a valley polarized metal phase; however, the band structures of

TABLE I. Binding energies (E_b) and interlayer distances (d) of different stacking configurations for $Mn_2P_2S_3Se_3/Sc_2CO_2$ heterostructures.

		$Mn_2P_2S_3Se_3/Sc_2CO_2(\uparrow)$		$Mn_2P_2S_3Se_3/Sc_2CO_2(\downarrow)$	
	Configuration	E_b (meV)	d (Å)	E_b (meV)	d (Å)
S-surface	Top-O	−286.86	2.58	−254.24	2.71
	Top-Sc	−226.90	2.88	−213.21	2.96
	Hollow	−180.01	3.26	−161.72	3.38
Se-surface	Top-O	−277.91	2.73	−256.86	2.80
	Top-Sc	−239.64	2.96	−226.97	3.05
	Hollow	−191.99	3.34	−176.09	3.45

$Mn_2P_2S_3Se_3/Sc_2CO_2$ P↓ exhibit valley polarized semiconductor characteristics.

To understand the origin of valley splitting for the $Mn_2P_2S_3Se_3/Sc_2CO_2$ heterostructure, we calculated the orbital-resolved band structure for the Mn atom d orbital, as shown in Fig. S5 in the Supplemental Material [44]. The CBM bands of the K and K′ points are mainly contributed by Mn $d_{xy}/d_{x^2-y^2}$ orbitals for all configurations, while the valence band maximum (VBM) bands of the K and K′ points for the P↑ and P↓ states are dominated by d_{z^2} and d_{xz}/d_{yz} orbitals, respectively. We then built an effective Hamiltonian model based on the SOC effect as a perturbation term. The SOC Hamiltonian can be described as

$$\hat{H}_{\mathrm{SOC}} = \lambda \hat{S} \cdot \hat{L} = \hat{H}^0_{\mathrm{SOC}} + \hat{H}^1_{\mathrm{SOC}}, \tag{1}$$

where $\hat{L}$ and $\hat{S}$ are orbital angular and spin angular operators, respectively, and $\hat{H}^0_{\mathrm{SOC}}$ and $\hat{H}^1_{\mathrm{SOC}}$ denote the interaction between the same spin states and between opposite spin states, respectively. Since the valley splitting mainly occurs at the CBM bands, for the $Mn_2P_2S_3Se_3/Sc_2CO_2$ heterostructure, we focus on the mechanism of the CBM valley splitting. Although the CBM is composed of spin-up and spin-down bands, they are degenerate. Therefore, we only consider the term $\hat{H}^0_{\mathrm{SOC}}$ and ignore the term $\hat{H}^1_{\mathrm{SOC}}$. Moreover, $\hat{H}^0_{\mathrm{SOC}}$ can be written in polar coordinates:

$$\hat{H}^0_{\mathrm{SOC}} = \lambda \hat{S}_{z'} \left(\hat{L}_z \cos\theta + \frac{1}{2}\hat{L}_+ e^{-i\phi} \sin\theta + \frac{1}{2}\hat{L}_- e^{+i\phi} \sin\theta \right). \tag{2}$$

In the out-of-plane magnetization case, $\theta = \phi = 0°$. The $\hat{H}^0_{\mathrm{SOC}}$ term can then be simplified as

$$\hat{H}^0_{\mathrm{SOC}} = \lambda \hat{S}_z \hat{L}_z. \tag{3}$$

Taking into account the orbital contribution around the CBM valleys and the C_{3v} symmetry, we take $|\psi_c^\tau\rangle = \frac{1}{\sqrt{2}}(|d_{xy}\rangle + i\tau|d_{x2-y2}\rangle) \otimes |\uparrow\rangle$ as the orbital basis for the CBM, where $\tau = \pm 1$ represents the valley index corresponding to K/K′. The energy levels of the valleys for the CBM can be written as $E_c^\tau = \langle\psi_c^\tau|\hat{H}^0_{\mathrm{SOC}}|\psi_c^\tau\rangle$. Then, the valley polarization can be expressed as

$$\begin{aligned} E_c^K - E_c^{K'} &= i\langle d_{xy}|\hat{H}^0_{\mathrm{SOC}}|d_{x2-y2}\rangle \\ &\quad - i\langle d_{x2-y2}|\hat{H}^0_{\mathrm{SOC}}|d_{xy}\rangle \approx 4\beta, \end{aligned} \tag{4}$$

where $\hat{L}_z|d_{xy}\rangle = -2i\hbar|d_{x2-y2}\rangle$, $\hat{L}_z|d_{x2-y2}\rangle = 2i\hbar|d_{xy}\rangle$, and $\beta = \lambda\langle d_{x2-y2}|\hat{S}_{z'}|d_{x2-y2}\rangle$.

To understand the physics mechanism of the Sc_2CO_2 polarization switching-driven valley polarized metal-semiconductor transition, we calculated the three-dimensional (3D) charge density difference and plane-averaged charge density difference ($\Delta\rho$), as shown in Figs. 3(b), 3(f), 3(d), and 3(h). The negative and positive values (blue and red areas) denote electron depletion and accumulation, respectively. Clearly, the $Mn_2P_2S_3Se_3/Sc_2CO_2$ P↑ system shows a notable charge transfer from $Mn_2P_2S_3Se_3$ to Sc_2CO_2. Conversely, in the $Mn_2P_2S_3Se_3/Sc_2CO_2$ P↓ case, the $Mn_2P_2S_3Se_3$ serves as an acceptor and accumulates electrons, whereas

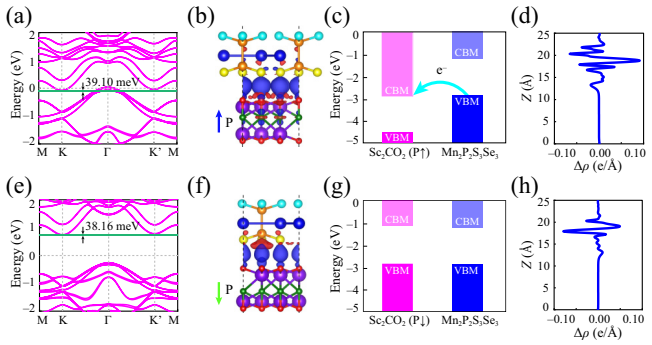

FIG. 3. Top-O configuration $Mn_2P_2S_3Se_3/Sc_2CO_2$ heterostructures for the S-surface. Band structures considering SOC under the (a) P↑ and (e) P↓ states. 3D charge density differences under the (b) P↑ and the (f) P↓ states. Band alignments of the (c) P↑ and (g) P↓ states. Plane-averaged charge density differences for the (d) P↑ and (h) P↓ states. The conduction-band valley splitting is indicated by the green shading.

the Sc_2CO_2 acts as a donor and loses electrons. In addition, we calculated the band alignments of the $Mn_2P_2S_3Se_3/Sc_2CO_2$ heterostructure. As shown in Figs. 3(c) and 3(g), the VBM and CBM are acquired from freestanding $Mn_2P_2S_3Se_3$ and Sc_2CO_2. In the Sc_2CO_2 P↑ case, the CBM of Sc_2CO_2 is lower than the VBM of $Mn_2P_2S_3Se_3$, and electrons tend to migrate from $Mn_2P_2S_3Se_3$ to Sc_2CO_2. Due to the inherent electric field, there is a potential difference of 1.84 eV between the two sides of Sc_2CO_2, resulting in obviously different band shifts in $Mn_2P_2S_3Se_3$ when it contacts the opposite sides. In the Sc_2CO_2 P↓ case, the VBM of Sc_2CO_2 is slightly above the VBM of $Mn_2P_2S_3Se_3$, leading to electron transfer from Sc_2CO_2 to $Mn_2P_2S_3Se_3$. Importantly, this is exactly consistent with the charge transfer.

The result for the Se-surface case is very similar to the S-surface case. In the absence of SOC, the spin-up and spin-down bands are degenerate, as shown in Fig. S6 in the Supplemental Material [44]. The system exhibits metallic properties aside from the hollow configuration for the $Mn_2P_2S_3Se_3/Sc_2CO_2$ P↑ case [see Figs. S6(a)–S6(c)] [44], while the $Mn_2P_2S_3Se_3/Sc_2CO_2$ P↓ case retains semiconductor properties [see Fig. S6(d–f)] [44]. When SOC is considered, as shown in Figs. 4(a), 4(e), and S7 [44], the CBM of the K and K′ points show a valley splitting of 34.16–39.53 meV. Moreover, Fig. S8 in the Supplemental Material shows the calculated projected band structures for the Mn atomic d orbital [44]. The CBM is dominated by the $d_{xy}/d_{x^2-y^2}$ orbital of the Mn atom for all configurations. In the comparison, the VBMs of the K and K′ points for the P↑ and P↓ cases are primarily contributed by the d_{z^2} and d_{xz}/d_{yz} orbitals, respectively. To further understand the electronic properties of Sc_2CO_2 in different polarization states, we investigated the 3D charge density difference [see Figs. 4(b) and 4(f)] and plane-averaged charge density difference [see Figs. 4(d) and 4(h)]. Clearly, the charge transfer occurs from $Mn_2P_2S_3Se_3$ to Sc_2CO_2 for the Sc_2CO_2 P↑ case. Conversely, when the polarization of Sc_2CO_2 transforms from P↑ to P↓, the charge transfer also switches from Sc_2CO_2 to $Mn_2P_2S_3Se_3$. We also investigated the band alignments of the $Mn_2P_2S_3Se_3/Sc_2CO_2$ heterostructure, as shown in Figs. 4(c) and 4(g). The VBM of $Mn_2P_2S_3Se_3$ is higher than the CBM of Sc_2CO_2, leading to charge transfer from $Mn_2P_2S_3Se_3$ to Sc_2CO_2 for the Sc_2CO_2 P↑ case. When the polarization is switched from P↑ to P↓, the VBM of Sc_2CO_2 will be slightly above the VBM of $Mn_2P_2S_3Se_3$, resulting in the direction of charge transfer also being switched. These results also mutually confirm the correctness of our calculations.

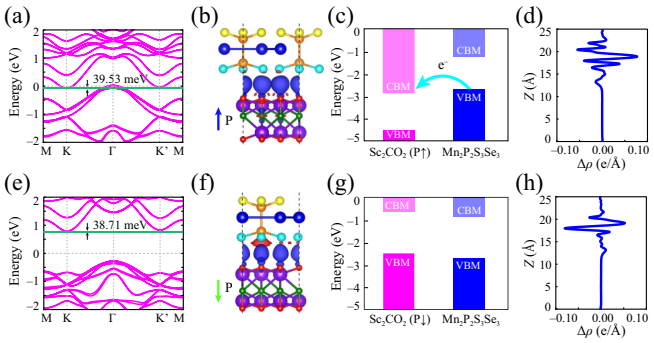

FIG. 4. Top-O configuration $Mn_2P_2S_3Se_3/Sc_2CO_2$ heterostructure for the Se-surface. Band structures considering SOC under the (a) P↑ and (e) P↓. 3D charge density difference under the (b) P↑ and (f) P↓ states. Band alignments of the (c) P↑ and (g) P↓ states. Plane-averaged charge density difference for the (d) P↑ and (h) P↓ states. The conduction band valley splitting is indicated by the green shading.

C. Nonlinear Hall effect and electronic property detection devices

Since the nonlinear Hall voltage is proportional to the BCD, and the BCD is highly dependent on symmetry, we analyze it in the context of the symmetries of the system. Monolayer $Mn_2P_2S_3Se_3$ has neither P nor T symmetry. First, we analyze the symmetry of the Berry curvature $\Omega_{n,d}$, where n is the band index. For the P symmetry, $\Omega_{n,d}$ is even, i.e., $\Omega_{n,d}(\mathbf{k}) = \Omega_{n,d}(-\mathbf{k})$. Conversely, $\Omega_{n,d}$ is odd under T symmetry, i.e., $\Omega_{n,d}(\mathbf{k}) = -\Omega_{n,d}(-\mathbf{k})$. Hence, there are nonzero BCD components in monolayer $Mn_2P_2S_3Se_3$.

The BCD is a 3 × 3 tensor, and D_{bd} is defined as

$$D_{bd} = \sum_n \int_k f_n(\mathbf{k}) \frac{\partial \Omega_{n,d}(\mathbf{k})}{\partial \mathbf{k}_b} = \sum_n \int_k \frac{\partial \epsilon_{kn}}{\partial \mathbf{k}_b} \Omega_{n,d}(\mathbf{k}) \frac{\partial f_n(\mathbf{k})}{\partial \epsilon_{kn}}, \tag{5}$$

where $f_n(\mathbf{k})$ is the Fermi-Dirac distribution, and $\Omega_{n,d}(\mathbf{k})$ is the Berry curvature. In 2D materials, only the z component of the Berry curvature is retained, namely

$$\Omega_{n,z}(\mathbf{k}) = -\sum_{n' \neq n} \frac{2\mathrm{Im}\,\langle \psi_{nk} \mid v_x \mid \psi_{n'k} \rangle \langle \psi_{n'k} \mid v_y \mid \psi_{nk} \rangle}{(E_{n'} - E_n)^2}. \tag{6}$$

The BCD is a pseudotensor determined by [25]

$$\mathbf{D} = \det(S) S \mathbf{D} S^{-1}, \tag{7}$$

where S represents the symmetric operation matrix of the point group. The magnetic point group of monolayer $Mn_2P_2S_3Se_3$ is $3m$. The magnetic point group $3m$ includes a threefold rotation C_3 symmetry along the z axis (C_{3z}), and three mirror reflections: perpendicular to the xy plane (M_{xy}), x axis (M_x), and y axis (M_y). The symmetric

operators of C_{3z}, M_{xy}, M_x, and M_y are

$$C_{3z} = \begin{pmatrix} \cos(2\pi/3) & -\sin(2\pi/3) & 0 \\ \sin(2\pi/3) & \cos(2\pi/3) & 0 \\ 0 & 0 & 1 \end{pmatrix}, \quad (8)$$

$$M_{xy} = \begin{pmatrix} 0 & -1 & 0 \\ -1 & 0 & 0 \\ 0 & 0 & 1 \end{pmatrix}, \quad (9)$$

$$M_x = \begin{pmatrix} -1 & 1 & 0 \\ 0 & 1 & 0 \\ 0 & 0 & 1 \end{pmatrix}, \quad (10)$$

$$M_y = \begin{pmatrix} 1 & 0 & 0 \\ 1 & -1 & 0 \\ 0 & 0 & 1 \end{pmatrix}. \quad (11)$$

For Eqs. (7)–(11), it is worth noting that only the D_{xz} component can exist for monolayer $Mn_2P_2S_3Se_3$ with the $3m$ magnetic point group [30,32]. Figure S9 of the Supplemental Material [44] exhibits the calculated BCD as a function of energy for monolayer $Mn_2P_2S_3Se_3$. Clearly, D_{xz} is very small since the band crossing is almost nonexistent in the -2 to 2 eV energy range.

When $Mn_2P_2S_3Se_3$ and Sc_2CO_2 form a heterostructure, the point group decreases from C_{3v} to C_{1h}. Consequently, only the M_y mirror symmetry is preserved. Therefore, the BCD component D_{xz} is still retained, and it is significantly enhanced. Figure 5 shows the calculated BCD components D_{xz} for the top-O configuration $Mn_2P_2S_3Se_3/Sc_2CO_2$ heterostructure. For the P↑ case [see Figs. 5(a) and 5(b)], D_{xz} has a nonzero value at the Fermi level. When the P switches to ↓, D_{xz} becomes zero. This change arises from the presence or absence of a band gap in the two polarization states. In addition, the D_{xz} value of P↑ is remarkably larger than that of P↓. Clearly, the value of D_{xz} reached 0.50 Å at $E_F + 1.477$ eV for the Se-surface. To understand the origin of this, we calculated the corresponding k-resolved Berry curvatures for the P↑ case, as shown in Figs. 5(e) and 5(f). It can clearly be seen that the contribution near the Γ point is very large. For the S-surface, the positive and negative Berry curvatures are almost equivalent, so D_{xz} is smaller. In contrast, the Se-surface has predominantly positive Berry curvature near the Γ point. Similarly, the k-resolved Berry curvatures were investigated for the P↓ case at $E_F - 0.891$ eV. In contrast to the P↑ case, the main contribution comes from the vicinity of the K and K′ points. Additionally, the S-surface exhibits significantly larger values than the Se-surface, which is consistent with the behavior of D_{xz}.

We calculate the anomalous Hall conductivity (AHC) using

$$\sigma'_{xy} = \sigma_{xy} \times \frac{l_z}{l_z^0}, \quad (12)$$

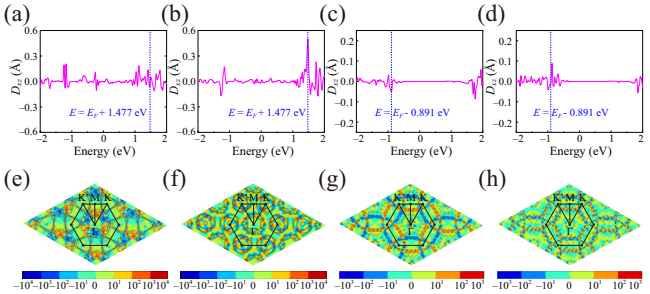

FIG. 5. Calculated BCD components D_{xz} of top-O configurations as a function of energy for the (a) S-surface $Mn_2P_2S_3Se_3/Sc_2CO_2$ heterostructure P↑, (b) Se-surface $Mn_2P_2S_3Se_3/Sc_2CO_2$ heterostructure P↑, (c) S-surface $Mn_2P_2S_3Se_3/Sc_2CO_2$ heterostructure P↓, and (d) Se-surface $Mn_2P_2S_3Se_3/Sc_2CO_2$ heterostructure P↓. 2D k-resolved Berry curvature Ω_z for the (e) S-surface $Mn_2P_2S_3Se_3/Sc_2CO_2$ heterostructure P↑ at $E_F + 1.477$ eV, (f) Se-surface $Mn_2P_2S_3Se_3/Sc_2CO_2$ heterostructure P↑ at $E_F + 1.477$ eV, (g) S-surface $Mn_2P_2S_3Se_3/Sc_2CO_2$ heterostructure P↓ at $E_F - 0.891$ eV, and (h) Se-surface $Mn_2P_2S_3Se_3/Sc_2CO_2$ heterostructure P↓ at $E_F - 0.891$ eV.

where σ_{xy} is the original AHC value from the WANNIER90 calculation, l_z is the height along the z direction that contains the vacuum layer, and l_z^0 is the height of the heterostructure. The calculation results are shown in Fig. S10 in the Supplemental Material [44]. We found that the AHC for both the S-surface and Se-surface P↑ heterostructures has nonzero values at the Fermi level. When the polarization of Sc_2CO_2 switches to downward, the AHC of the S- or Se-surface configurations becomes zero. This is due to the presence or absence of a band gap in the two polarization states.

The manipulation and detection of charge, spin, or valley is the basis of realizing electronic, spintronic, and valleytronic devices. Similarly, the valley polarized metal-semiconductor transition can be detected and manipulated using valleytronic devices. Our calculation results show that the NHE can effectively reflect the valley polarized metal-semiconductor phase transition. If D_{xz} is nonzero for

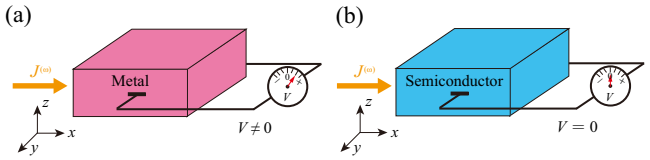

FIG. 6. Schematics of the electronic property detection device using the NHE. The driving current flows along the x axis, and the nonlinear Hall voltage is generated along the y axis, which is determined by the electronic properties. The nonlinear Hall voltage is (a) nonzero for the valley polarized metal and (b) zero for the valley polarized semiconductor.

the valley polarized metal, in the $Mn_2P_2S_3Se_3/Sc_2CO_2$ heterostructure P↑ case, a nonzero Hall signal will be detected along the y axis, as shown in Fig. 6(a). Conversely, when the ferroelectric polarization of Sc_2CO_2 switches to P↓, the valley polarized semiconductor cannot generate the nonlinear Hall voltage due to the absence of bands near the Fermi level [see Fig. 6(b)]. The detection and manipulation of the valley polarized metal-semiconductor transition will be vital for advancing electronics, spintronics, and valleytronics.

IV. CONCLUSION

In summary, we systematically investigated the stability, magnetic ground state, electronic properties, and NHE for vdW $Mn_2P_2S_3Se_3/Sc_2CO_2$ heterostructures. We find that monolayer $Mn_2P_2S_3Se_3$ is a robust AFM valley semiconductor for the Coulomb repulsion U. After forming a heterostructure with Sc_2CO_2, the valley splitting is further enhanced. Importantly, when the $Mn_2P_2S_3Se_3/Sc_2CO_2$ heterostructure is in the P↑ state, it exhibits a valley polarization metallic property; however, when the ferroelectric polarization of Sc_2CO_2 transforms from P↑ to P↓, the system undergoes a phase transition from a valley-polarized metal to a valley-polarized semiconductor. It is worth noting that this phenomenon exists for both the S-surface and Se-surface configurations. Moreover, we also find that the BCD can be effectively tuned by switching the polarization direction of Sc_2CO_2. Based on this, we propose that NHE devices could be employed to detect valley polarized metal-semiconductor transitions. The key to designing electronic devices is to construct binary logic switching states. Similar to spin, valley represents a new type of freedom, and different valley polarization states can be used to encode and store information. The phase transition from a valley-polarized semiconductor to a metal state, facilitated by a ferroelectric substrate, provides a novel platform for the realization of next-generation nonvolatile information-storage devices. Our findings are expected to broaden the application scenarios of the NHE.

Note added. During the review of our paper, the antiferromagnetic ferrovalley material is proposed [47], and the valley polarization induced by lattice symmetry breaking [48].

ACKNOWLEDGMENTS

This work is supported by the National Natural Science Foundation of China (Grants No. 12474238 and 12004295). P.L. also acknowledges support from China's Postdoctoral Science Foundation funded project (Grant No. 2022M722547), the Fundamental Research Funds for the Central Universities (Grant No. xxj03202205), the Open Project of State Key Laboratory of Surface Physics (Grant No. KF2024_02), and the Open Project of State Key Laboratory of Silicon and Advanced Semiconductor Materials (Grant No. SKL2024-10).

[1] G. E. Moore, Cramming more components onto integrated circuits, Proc. IEEE **86**, 82 (1998).
[2] A. D. Franklin, Nanomaterials in transistors: From high-performance to thin-film applications, Science **349**, aab2759 (2015).
[3] M. Wang, S. Cai, C. Pan, C. Wang, X. Lian, Y. Zhuo, K. Xu, T. Cao, X. Pan, B. Wang, S. J. Liang, J. J. Yang, P. Wang, and F. Miao, Robust memristors based on layered two-dimensional materials, Nat. Electron. **1**, 130 (2018).
[4] X. Liu and M. C. Hersam, 2D materials for quantum information science, Nat. Rev. Mater. **4**, 669 (2019).
[5] P. Li, X. S. Zhou, and Z. X. Guo, Intriguing magnetoelectric effect in two-dimensional ferromagnetic/perovskite oxide ferroelectric heterostructure, npj Comput. Mater. **8**, 20 (2022).
[6] P. Li, J. Z. Zhang, Z. X. Guo, T. Min, and X. R. Wang, Intrinsic anomalous spin Hall effect, Sci. China Phys. Mech. **66**, 227511 (2023).
[7] A. Zhang, Z. Gong, Z. Zhu, A. Pan, and M. Chen, Effects of the substrate-surface reconstruction and orientation on the spin valley polarization in $MoTe_2$/EuO, Phys. Rev. B **102**, 155413 (2020).
[8] Y. Liu, X. Duan, H. Shin, S. Park, Y. Huang, and X. Duan, Promises and prospects of two-dimensional transistors, Nature **591**, 43 (2021).
[9] R. Quhe, Z. Di, J. Zhang, Y. Sun, L. Zhang, Y. Guo, S. Wang, and P. Zhou, Asymmetric conducting route and potential redistribution determine the polarization-dependent conductivity in layered ferroelectrics, Nat. Nanotechnol. **19**, 173 (2024).
[10] T. Latychevskaia, D. A. Bandurin, and K. S. Novoselov, A new family of septuple-layer 2D materials of $MoSi_2N_4$-like crystals, Nat. Rev. Phys. **6**, 426 (2024).
[11] W. Y. Tong, S. J. Gong, X. Wan, and C. G. Duan, Concepts of ferrovalley material and anomalous valley Hall effect, Nat. Commun. **7**, 13612 (2016).
[12] P. Li, C. Wu, C. Peng, M. Yang, and W. Xun, Multifield tunable valley splitting in two-dimensional MXene Cr_2COOH, Phys. Rev. B **108**, 195424 (2023).
[13] Y. Liu, Y. Feng, Y. Dai, B. Huang, and Y. Ma, Engineering layertronics in two-dimensional ferromagnetic multiferroic lattice, Nano Lett. **24**, 3507 (2024).
[14] P. Li, B. Liu, S. Chen, W. X. Zhang, and Z. X. Guo, Progress on two-dimensional ferovalley materials, Chin. Phys. B **33**, 017505 (2024).
[15] J. Zhao, Y. Feng, Y. Dai, B. Huang, and Y. Ma, Ferroelectrovalley in two-dimensional multiferroic lattices, Nano Lett. **24**, 10490 (2024).
[16] G. Yu, J. Ji, C. Xu, and H. J. Xiang, Bilayer stacking ferrovalley materials without breaking time-reversal and spatial-inversion symmetry, Phys. Rev. B **109**, 075434 (2024).
[17] D. MacNeill, C. Heikes, K. F. Mak, Z. Anderson, A. Kormanyos, V. Zolyomi, J. Park, and D. C. Ralph, Breaking of

valley degeneracy by magnetic field in monolayer $MoSe_2$, Phys. Rev. Lett. **114**, 037401 (2015).

[18] M. U. Rehman, Z. U. Rahman, and M. Kiani, Emerging spintronic and valleytronic phenomena in noncentrosymmetric variants of the Kane-Mele $X_4Y_2Z_6$ materials family (X = Pt, Pd, Ni; Y = Hg, Zn, Cd; Z = S, Se, Te), Phys. Rev. B **109**, 165424 (2024).

[19] W. Xun, C. Wu, H. Sun, W. Zhang, Y. Z. Wu, and P. Li, Coexisting magnetism, ferroelectric, and ferrovalley multiferroic in stacking-dependent two-dimensional materials, Nano Lett. **24**, 3541 (2024).

[20] K. Shao, H. Geng, E. Liu, J. L. Lado, W. Chen, and D. Y. Xing, Non-Hermitian moiré valley filter, Phys. Rev. Lett. **132**, 156301 (2024).

[21] H. Hu, W. Y. Tong, Y. H. Shen, X. Wan, and C. G. Duan, Concepts of the half-valley-metal and quantum anomalous valley Hall effect, npj Comput. Mater. **6**, 129 (2020).

[22] W. Pan, Tuning the magnetic anisotropy and topological phase with electronic correlation in single-layer H-$FeBr_2$, Phys. Rev. B **106**, 125122 (2022).

[23] Z. He, R. Peng, X. Feng, X Xu, Y. Dai, B. Huang, and Y. Ma, Two-dimensional valleytronic semiconductor with spontaneous spin and valley polarization in single-layer Cr_2Se_3, Phys. Rev. B **104**, 075105 (2021).

[24] K. Wang, Y. Li, H. Mei, P. Li, and Z. X. Guo, Quantum anomalous Hall and valley quantum anomalous Hall effects in two-dimensional d^0 orbital XY monolayers, Phys. Rev. Mater. **6**, 044202 (2022).

[25] Y. Wu, J. Tong, L. Deng, F. Luo, F. Tian, G. Qin, and X. Zhang, Coexisting ferroelectric and ferrovalley polarizations in bilayer stacked magnetic semiconductors, Nano Lett. **23**, 6226 (2023).

[26] P. Li, X. Yang, Q. S. Jiang, Y. Z. Wu, and W. Xun, Built-in electric field and strain tunable valley-related multiple topological phase transitions in $VSiXN_4$ (X = C, Si, Ge, Sn, Pb) monolayers, Phys. Rev. Mater. **7**, 064002 (2023).

[27] S. D. Guo, L. Zhang, Y. Zhang, P. Li, and G. Wang, Large spontaneous valley polarization and anomalous valley Hall effect in antiferromagnetic monolayer Fe_2CF_2, Phys. Rev. B **110**, 024416 (2024).

[28] I. Sodemann and L. Fu, Quantum nonlinear hall effect induced by berry curvature dipole in time-reversal invariant materials, Phys. Rev. Lett. **115**, 216806 (2015).

[29] T. Low, Y. Jiang, and F. Guinea, Topological currents in black phosphorus with broken inversion symmetry, Phys. Rev. B **92**, 235447 (2015).

[30] R. C. Xiao, D. F. Shao, Z. Q. Zhang, and H. Jiang, Two-dimensional metals for piezoelectriclike devices based on berry-curvature dipole, Phys. Rev. Appl. **13**, 044014 (2020).

[31] N. N. Zhao, Z. F. Ouyang, P. H. Sun, J. F. Zhang, K. Liu, and Z. Y. Lu, Nonlinear Hall effect and potential Ising superconductivity in monolayer MXene heterostructure of T-Mo_2C/H-Mo_2C, Phys. Rev. B **108**, 035140 (2023).

[32] C. Wang, Y. Gao, and D. Xiao, Intrinsic nonlinear Hall effect in antiferromagnetic tetragonal CuMnAs, Phys. Rev. Lett. **127**, 277201 (2021).

[33] D. Kaplan, T. Holder, and B. Yan, General nonlinear Hall current in magnetic insulators beyond the quantum anomalous Hall effect, Nat. Commun. **14**, 3053 (2023).

[34] R. Chen, Z. Z. Du, H. P. Sun, H. Z. Lu, and X. C. Xie, Nonlinear Hall effect on a disordered lattice, Phys. Rev. B **110**, L081301 (2024).

[35] P. E. Blochl, Projector augmented-wave method, Phys. Rev. B **50**, 17953 (1994).

[36] G. Kresse and J. Furthmuller, Efficient iterative schemes for ab initio total-energy calculations using a plane-wave basis set, Phys. Rev. B **54**, 11169 (1996).

[37] J. P. Perdew, K. Burke, and M. Ernzerhof, Generalized gradient approximation made simple, Phys. Rev. Lett. **77**, 3865 (1996).

[38] S. Grimme, J. Antony, S. Ehrlich, and H. Krieg, A consistent and accurate ab initio parameterization of density functional dispersion correction (DFT-D) for the 94 elements H-Pu, J. Chem. Phys. **132**, 154104 (2010).

[39] A. Togo and I. Tanaka, First principles phonon calculations in materials science, Scr. Mater. **108**, 1 (2015).

[40] A. A. Mostofi, J. R. Yates, Y. S. Lee, I. Souza, D. Vanderbilt, and N. Marzari, wannier90: A tool for obtaining maximally-localised Wannier functions, Commput. Phys. Commun. **178**, 685 (2008).

[41] A. A. Mostofi, J. R. Yates, G. Pizzi, Y. S. Lee, I. Souza, D. Vanderbilt, and N. Marizari, An updated version of wannier90: A tool for obtaining maximally-localised Wannier functions, Commput. Phys. Commun. **185**, 2309 (2014).

[42] P. Li, X. Li, J. Feng, J. Ni, Z. X. Guo, and H. Xiang, Origin of zigzag antiferromagnetic orders in XPS_3 (X = Fe, Ni) monolayers, Phys. Rev. B **109**, 214418 (2024).

[43] A. Chandrasekaran, A. Mishra, and A. K. Singh, Ferroelectricity, antiferroelectricity, and ultrathin 2D electron/hole gas in multifunctional monolayer MXene, Nano Lett. **17**, 3290 (2017).

[44] See Supplemental Material at http://link.aps.org/supplemental/10.1103/PhysRevApplied.23.034032 for the band structure of monolayer $Mn_2P_2S_3Se_3$ without considering SOC, the $Mn_2P_2S_3Se_3/Sc_2CO_2$ heterostructures configurations for the Se-surface, the spin-polarized band structures of $Mn_2P_2S_3Se_3/Sc_2CO_2$ heterostructures for the S-surface, the band structures of $Mn_2P_2S_3Se_3/Sc_2CO_2$ heterostructures for the S-surface considering SOC, the projected band structures of $Mn_2P_2S_3Se_3/Sc_2CO_2$ heterostructures for the S-surface considering SOC, the spin-polarized band structures of $Mn_2P_2S_3Se_3/Sc_2CO_2$ heterostructures for the Se-surface, the band structures of $Mn_2P_2S_3Se_3/Sc_2CO_2$ heterostructures for the Se-surface considering SOC, the projected band structures of $Mn_2P_2S_3Se_3/Sc_2CO_2$ heterostructures for the Se-surface considering SOC, the calculated BCD components D_{xz} as a function of energy for monolayer $Mn_2P_2S_3Se_3$, the calculated anomalous Hall conductivity of the top-O configurations, the energy difference between the ferromagnetic and antiferromagnetic states and the MAE for monolayer $Mn_2P_2S_3Se_3$, the energy difference between the ferromagnetic and antiferromagnetic states for different stacking configurations of $Mn_2P_2S_3Se_3/Sc_2CO_2$ heterostructures, and the MAE of different stacking configurations for $Mn_2P_2S_3Se_3/Sc_2CO_2$ heterostructures.

[45] P. Li and T. Y. Cai, Two-dimensional transition-metal oxides Mn_2O_3 realized the quantum anomalous Hall effect, J. Phys. Chem. C **124**, 12705 (2020).

[46] W. Du, R. Peng, Z. He, Y. Dai, B. Huang, and Y. Ma, Anomalous valley Hall effect in antiferromagnetic monolayers, npj 2D Mater. Appl. **6**, 11 (2020).

[47] Y. Wang, H. Sun, C. Wu, W. Zhang, S.-D. Guo, Y. She, and P. Li, Multifield tunable valley splitting and anomalous valley Hall effect in two-dimensional antiferromagnetic MnBr, Phys. Rev. B **111**, 085432 (2025).

[48] C. Wu, H. Sun, P. Dong, Y.-Z. Wu, and P. Li, Coexisting triferroic and multiple types of valley polarization by structural phase transition in two-dimensional materials, Adv. Funct. Mater. **35**, 2501506 (2025).